

# Development of fiber Bragg grating as a sensor based on Mach-Zehnder interferometer and development of optical fiber instruments: A review

**Bunga Meyzia**

Department of Physics, Universitas Riau, Pekanbaru 28293, Indonesia

## ABSTRACT

Over the past few decades optical sensor has experienced significant development. The utilization of fiber Bragg grating for the detection of various parameter such as stress, strain, displacement, temperature, refractive index, humidity, pressure and vibration by measuring the changes in wavelength, polarization, intensity of light passing through the sensing region and phase. This review discusses the development of optical sensors using the Mach-Zehnder interferometer which is being frequently used for sensing applications due to their geometric and flexible construction. This review would be useful for the researchers to develop miniaturize fiber devices and instrument with enhanced sensing performance.

## ARTICLE INFO

### Article history:

Received Apr 14, 2025

Revised May 17, 2025

Accepted Jun 20, 2025

### Keywords:

Fiber Bragg Grating  
Interferometer  
Mach-Zehnder  
Optical Fiber Sensor  
Sensing Instruments

*This is an open access  
article under the [CC BY](#)  
license.*



\* **Corresponding Author**

E-mail address: [bungameyzia@gmail.com](mailto:bungameyzia@gmail.com)

## 1. INTRODUCTION

Fiber optic sensors have been the center of research for decades. Various types of fiber optic sensors have been developed, such as magnetic field sensors, salinity sensors) [1-3], molecular sensors, tilt sensors, pressure sensors and ultrasonic sensors [4]. Fiber optic sensors have several advantages over conventional sensors such as high sensitivity, can measure at long distances, multiplexing, able to measure strain, can detect temperature shifts along the length of the fiber [5]. To measure the stress distributed along the length of the optical fiber, several techniques have been used such as fiber Bragg grating (FBG) sensors and interferometer-based sensors (Fabry-Perot and Mach-Zehnder) [6].

Fiber optic sensors based on interferometer structures have undergone significant development because they have an important role in monitoring several parameters such as physical, chemical and biological parameters [7]. The Mach-Zehnder sensor works based on the intensity of the phase difference variation illuminated by two separate rays from the same light source [8]. Different configurations of Mach-Zehnder interferometer (MZI) combined with FBG have been developed as a measuring medium for changes in refractive index and temperature, including the shape of the core structure that shifts in the MZI [9, 10]. However, sensors with very high sensitivity measurements still present their own challenges. This paper provides and summarizes the development of interferometer-based fiber optic sensor sensitivity.

## 2. LITERATURE REVIEW

### 2.1. FBG Sensor Principle in Temperature and Strain Measurement

#### 2.1.1. FBG Thermal Characterization

FBG is a cyclic modulation of the refractive index formed by exposure to UV radiation along the fiber core at a finite length of optical fiber [11, 12]. When light with a wide band propagates through an optical fiber, the grating acts as a narrowband filter to reflect the peak wavelength known as the Bragg wavelength [13-15]. The Bragg wavelength can be understood as:

$$\lambda_B = 2n\Lambda \quad (1)$$

where,  $\lambda_B$  is the Bragg wavelength reflected by the FBG,  $n$  is the effective refractive index and  $\Lambda$  is the lattice period [12].

Temperature sensors are the most common parameters used in most applications. Conventional temperature sensors such as thermocouples, large resistance temperature detectors and thermostats have a low operating range and are not resistant to electromagnetic waves [16, 17]. FBG sensors are a good solution because they have low thermal conductivity, are small in size and are very sensitive to electromagnetic waves [18, 19]. The use of thermal effects is the main cause of temperature sensitivity in FBGs [20]. In FBG sensors, the shift in the Bragg wavelength is caused by changes in temperature  $T$ . By deriving Equation (1) [15], the relationship between changes in wavelength and changes in temperature can be seen with:

$$\frac{\Delta\lambda}{\lambda} = \frac{1}{n_{eff}} \frac{dn_{eff}}{dT} \Delta T + \frac{1}{\Lambda} \frac{d\Lambda}{dT} \Delta T \quad (2)$$

$$\frac{\Delta\lambda}{\lambda} = (\epsilon_i + \alpha) \Delta T \lambda_B = 2n\Lambda \quad (3)$$

where,  $\Delta\lambda/\lambda$  is the normalized resonance shift due to temperature changes,  $\epsilon_i$  is the thermo optical coefficient, and  $\alpha$  is the thermal expansion coefficient. At a wavelength of 1330 nm, the values of  $\epsilon_i$  and  $\alpha$  in silica are  $6.6 \times 10^{-6} / ^\circ\text{C}$  and  $0.55 \times 10^{-6} / ^\circ\text{C}$ , so the temperature sensitivity value obtained is  $0.0094 \text{ nm}/^\circ\text{C}$ . The reflectance value of germanium doped by silica in FBG becomes low at high temperatures [21, 22]. Measurement of very high temperature values is very difficult to obtain so that research in developing sensitivity levels through FBG is very necessary in various applications [23].

In some main structures, the wavelength shift value of the bound structure with the unbound one caused by the induction of different temperature changes [24]. The unbound wavelength shift can be found by substituting the temperature change  $T$  into the equation:

$$\Delta\lambda_B = k_T \Delta T \lambda_B = \left\{ \left[ 1 - \frac{1}{2} n_0^2 (p_{11} + 2p_{12}) \right] \alpha_f \Delta T \right\} \quad (4)$$

where,  $n_0$  is the refractive index,  $p_{11}$  and  $p_{12}$  are Pockel constants,  $\alpha_f$  is the thermal expansion coefficient [25]. Measurement of the shift in the bound Bragg wavelength caused by temperature changes can be associated with the thermal strain  $T$  due to the mismatch of the thermal expansion value between the optical fiber and the main structure. The thermal strain value can be found through the equation [13]:

$$\epsilon_T = \frac{(\alpha_h - \alpha_f) \Delta T}{E_f \left( \frac{\pi r_f^2}{2hr_p E_h} + \frac{1}{E_f} \right)} \left[ 1 - \frac{\cosh(\lambda_1 x)}{\cosh(\lambda_1 L_f)} \right] + \alpha_f \Delta T \quad (5)$$

$$\lambda_1 = \sqrt{\left[ \frac{2r_p}{\pi r_f^2} \left( \frac{\pi r_f^2}{2hr_p E_h} + \frac{1}{E_f} \right) \int_0^{\cos^{-1} \frac{b}{r_p}} \frac{1}{\frac{r_p(1-\sin\theta)}{G_a} + \frac{r_p}{G_p} \ln\left(\frac{r_p}{r_f}\right)} d\theta \right]} \quad (6)$$

### 2.1.2. FBG Strain Mechanics Characterization

The use of FBG sensors for strain changes that occur depends on the shape of the structure and the nature of the material being passed [26, 27]. The mechanical stress transmitted to the FBG sensor from the material used can be seen in the equation:

$$\varepsilon_M = \frac{\varepsilon_0}{E_f \left( \frac{\pi r_f^2}{2hr_p E_h} + \frac{1}{E_f} \right)} \left[ 1 - \frac{\cosh(\lambda_1 x)}{\cosh(\lambda_1 L_f)} \right] \quad (7)$$

where,  $\varepsilon_0$  is the mechanical strain. The shift of the Bragg wavelength in the FBG bound to the structure can be determined by substituting Equation (6) into the equation below:

$$\frac{\Delta\lambda_B}{\lambda_B} = k_\varepsilon \varepsilon + k_T \Delta T \quad (8)$$

where,  $\varepsilon$  is the mechanical strain, the resulting Bragg wavelength shift equation becomes:

$$\Delta\lambda_B = k_\varepsilon \varepsilon_M \lambda_B \quad (9)$$

### 2.1.3. Characterization of Temperature Changes and Strain Mechanics

The use of the superposition principle creates a shift in the FBG Bragg wavelength relative to the main structure that has variations in temperature and mechanical strain, so that it can be explained by adding Equations (8) and (9) into [28]:

$$\frac{\Delta\lambda_B}{\lambda_B} = [k_\varepsilon \varepsilon_T + k_T \Delta T] \lambda_B + k_\varepsilon \varepsilon_M \lambda_B \quad (10)$$

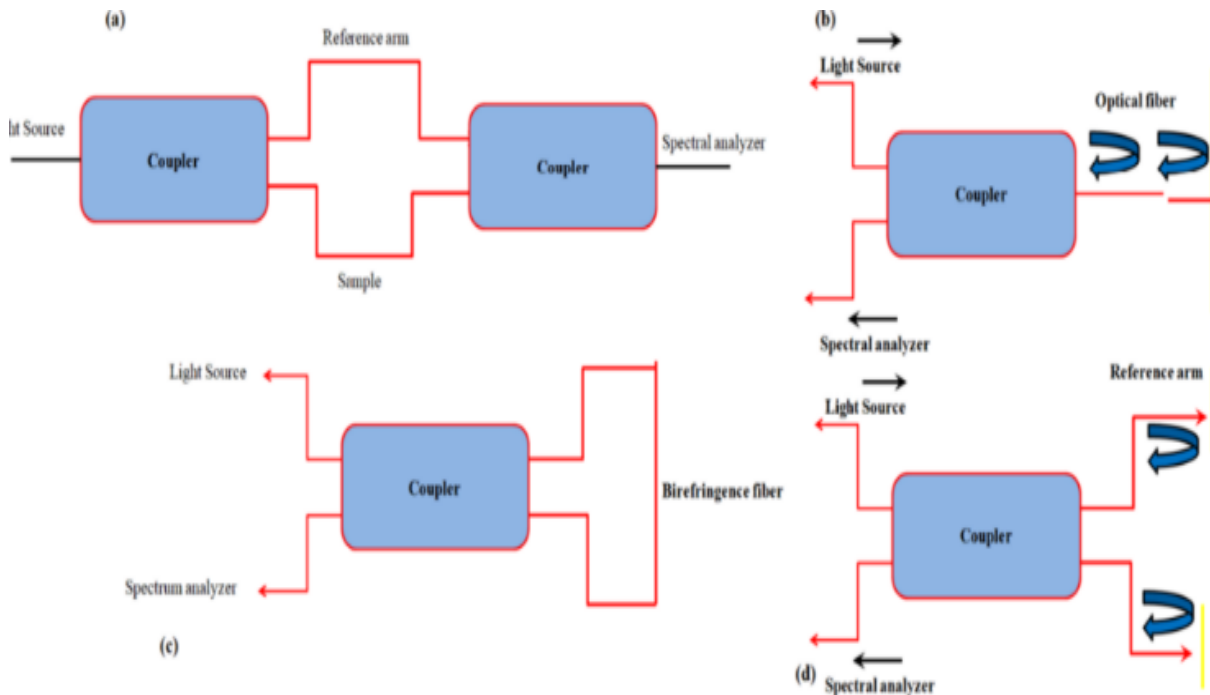


Figure 1. Interferometer form.

## 2.2. Sensor Form and Development Using MZI

### 2.2.1. Interferometer

The use of fiber optic sensor-based interferometers has experienced significant development in various applications. The use of this interferometer sensor depends on the high-order mode and the

fundamental mode that produces changes in the resonance wavelength. The spectrum of the phase transition that depends on the difference in the optical path length in the interference mode can be written as follows:

$$\Phi = \frac{2\pi}{\lambda} (\delta n_{eff}) L \quad (11)$$

where,  $L$  is the length of the sensor,  $\lambda$  is the wavelength and the refractive index difference between the higher order and cladding modes.

The sensor arm and the reference arm are the two main components in the interferometer sensor. The light passing through the FBG is divided into two different paths, where the light propagates through the sensor arm that can be disturbed, and the other light propagates through the reference arm that is isolated from the sensor medium. The dependence between the phase and the out-of-phase conditions between the two arms, produces destructive and constructive interference. This can show the phase difference due to the influence of the surrounding environment. Mach-Zehnder [29, 30], Michelson [31, 32], Fabry-Perot [33], Sagnac [30, 34] and interferometers are usually used based on the modulated phase conditions as shown in Figure 1.

### 2.2.2. MZI

FBS sensors based on MZI are currently widely developed in various sensor applications because they have flexible configurations. This sensor works to measure the phase shift between two rays. The length of the sensor and reference arms are the same but have a difference in optical path length which produces interference [35, 36]. This application is used by wearing the sensor arm in the surrounding environment while the reference arm remains isolated. Changes in one of the surrounding parameters induce a phase difference and this phase shift produces constructive and destructive interference patterns. Generally, MZI is based on multimode interference which can be shown in Figure 2.

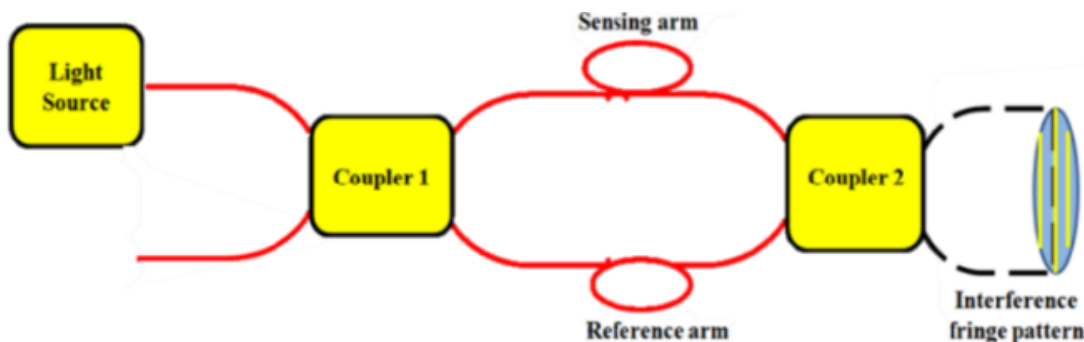


Figure 2. MZI [20].

The output intensity of the interference pattern can be written as:

$$I = I_1 + I_2 + 2\sqrt{I_1 I_2} \cos\Phi \quad (12)$$

where,  $I_1$  and  $I_2$  are the intensities of the propagating light and the phase difference can be calculated by  $\Phi = 2\pi/\lambda(\Delta n_{eff})L$  which is the same as the formula for Equation (11) [37-40].

## 3. RESEARCH METHODOLOGY

### 3.1. Structure and Principle of FBG sensor on MZI

#### 3.1.1. Sensor Fabrication

The combined development of MZI and FBG sensors is fabricated according to Figure 3. In the figure, the sensor consists of leading SMF (8.2 micrometers, 12.5 micrometers) trapezoidal

structure 1, sensing area (middle part of SMF), trapezoidal structure 2, output SMF and FBG. The trapezoidal structure is fabricated using a fusion splicer (FITELE S178C).

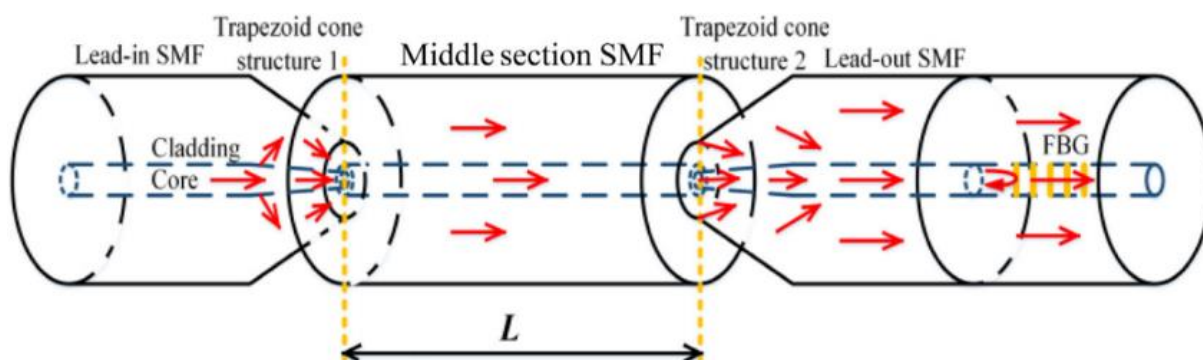


Figure 3. Schematic of FBG Sensor based on MZI.

The length of the SMF is stretched using an arc discharge to form a down-taper (the discharge intensity value is 3 bits and the discharge time is 1500 ms). The length of the down-taper  $Z$  is about  $606 \mu\text{m}$  and the width  $D$  is about  $44 \mu\text{m}$  as shown in Figure 4 (a). The middle region of the down-taper is thinly sliced by a fiber cleaver on an optical lens (Olympus DSX110) to form a trapezoid structure as shown in Figure 4 (b). The optical lens can magnify up to  $20 \times 10$  times and can clearly observe the same trapezoid structure shape within some experimental errors. The two trapezoids were welded to the center of the SMF using a fusing welder in manual welding (the discharge intensity was 90 bits and the discharge time was 1300 ms each) as shown in Figure 4 (c).

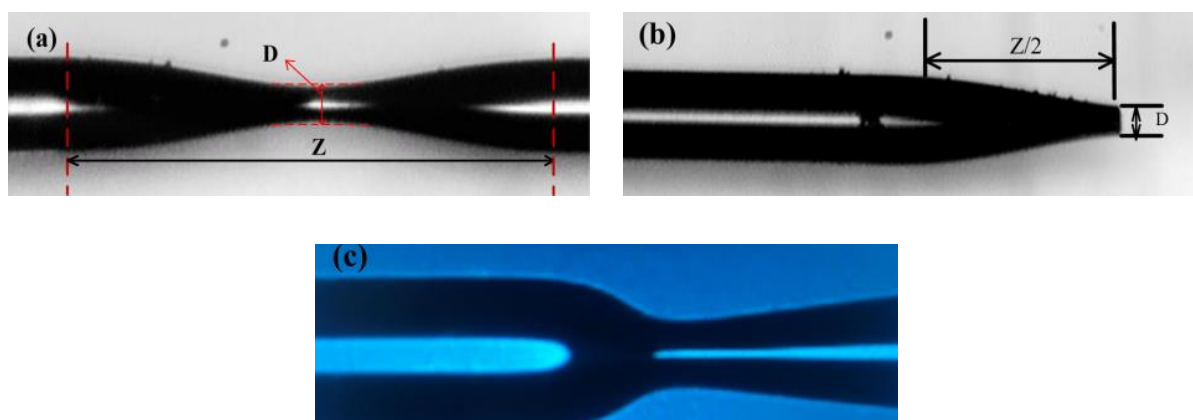


Figure 4. Image for: (a) image of the down-taper  $Z$ ; (b) image of the trapezoid structure; and (c) image of the splicing area between the trapezoid and the SMF.

### 3.1.2. MZI Simulation

One of the simulations that uses MZI as an interferometer is a simulation using the beam propagation method (BPM). This simulation is used with varying lengths to obtain the optical field distribution of the MZI. This simulation uses an input wavelength of  $1550 \text{ nm}$ , a refractive index of 1.0 and a cross-sectional length of the SMF, namely 1 cm, 3 cm, 5 cm, which can be seen in Figure 5.

In the figure, it can be seen that light passes through the cladding when light is transmitted to the trapezoid structure, so that the cladding mode appears. The cladding mode and core mode simultaneously transmit light in the middle of SMF. The coupling mode appears because the light passes through the trapezoid structure 2 as a beam combiner. The results of this simulation show that the energy of MZI with SMF in the middle of 3 cm changes in the core and cladding. This causes more modes in the cladding that can be stimulated by MZI with SMF in the middle of 3 cm. In addition to the simulation results, in the experiment, the difference in energy loss and extinction values

must also be considered. Due to several factors above, the length of the middle part of SMF in the experiment is 3 cm.

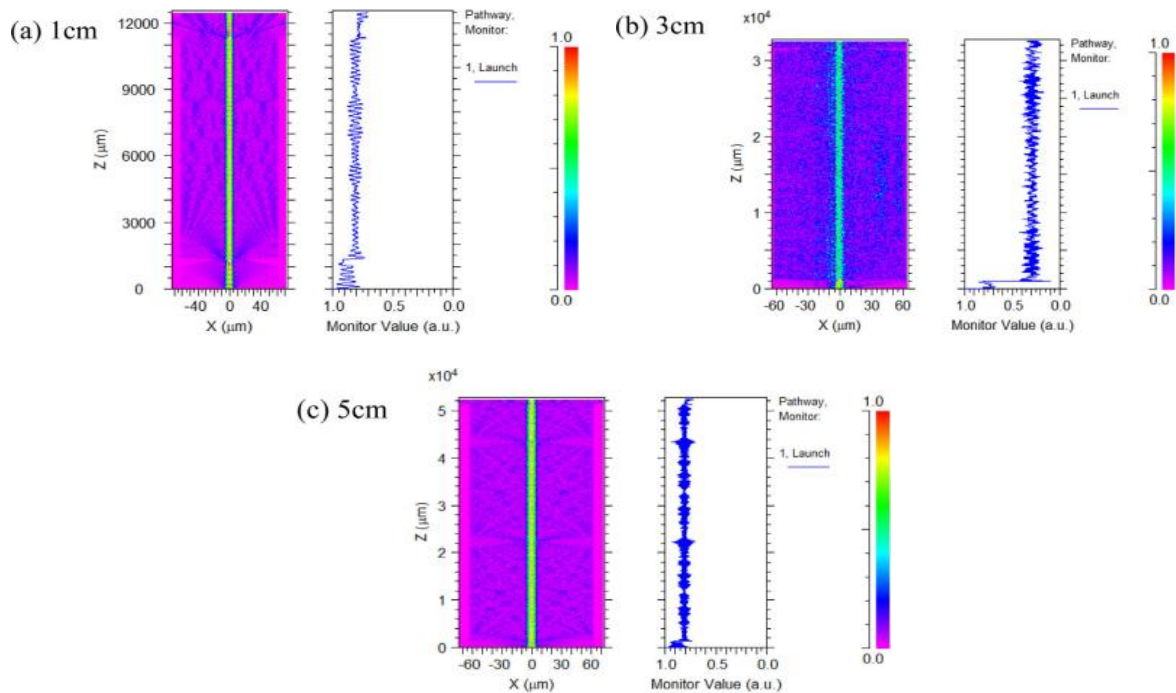


Figure 5. Simulation of optical field distribution in MZI: (a) variation of 1 cm in the middle area of SMF; (b) variation of 3 cm in the middle area of SMF; and (c) variation of 5 cm in the middle area of SMF.

### 3.1.3. Sensor Principle

The use of transmission characteristics in the interferometer can understand the spatial frequency spectrum of the MZI in experiments with a temperature of 25°C and a refractive index of ~ 1.0 which can be explained using the fast fourier transform (FFT) shown in Figure 6.

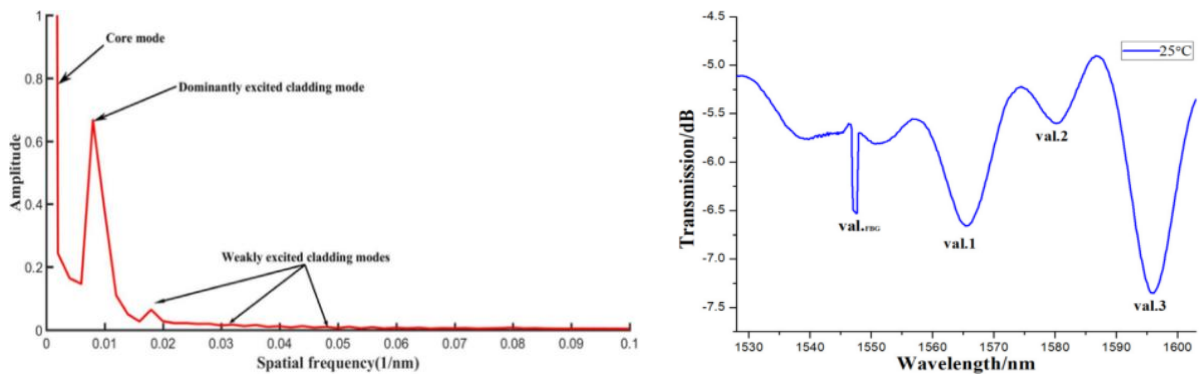


Figure 6. Spatial frequency spectrum of MZI.

The figure shows that there is one dominant excited cladding mode and several weakly excited cladding modes in the spatial frequency spectrum. Interference mainly occurs between the dominant cladding mode and the core mode, while the interference between the weak cladding mode and the core mode can be ignored because it has a low intensity. The reference intensity can be found by equation [11]:

$$I = I^{co} + \sum 2\sqrt{I^{co} + I^{cl}} \cos \frac{2\pi\Delta n_{eff}L}{\lambda} \tag{13}$$

where,  $I^{co}$  and  $I^{cl}$  are the light intensities of the core mode and cladding mode.  $L$  is the length of the center region of the SMF.

The interference wavelength can be obtained through the equation:

$$\lambda_{val}^{MZI} = \frac{2\Delta n_{eff}L}{2k+1} \quad (14)$$

where, the value of  $k$  is an integer.

The effective refractive index values in the core and cladding modes change when the ambient temperature changes, while the change in refractive index only affects the effective refractive index of the cladding mode. Then the variation of the value of  $\lambda_{val}^{MZI}$  with changes in ambient temperature and refractive index can be concluded from Equation (14) as:

$$\lambda_{val}^{MZI} + \Delta\lambda_{val}^{MZI} = \frac{2L}{2k+1} \left[ (n_{eff}^{co} + \xi^{co}n_{eff}^{co}\Delta T) - (n_{eff}^{cl} + \xi^{co}n_{eff}^{cl}\Delta T + \rho n_{eff}^{cl}\Delta RI) \right] \quad (15)$$

where,  $\Delta T$  and  $\Delta RI$  are the ambient temperature difference and refractive index,  $\xi^{co}$  and  $\xi^{cl}$  are the thermo-optic coefficients of the core mode and cladding mode,  $\rho$  is the effective coefficient of the variation of  $n_{eff}^{cl}$  caused by the refractive index.  $\Delta\lambda_{val}^{MZI}$  is the variation of  $\lambda_{val}^{MZI}$  obtained from the refractive index and temperature. Based on Equation (14), then  $\Delta\lambda_{val}^{MZI}$  can be explained in more detail by the equation:

$$\Delta\lambda_{val}^{MZI} = \frac{2L}{2k+1} \left[ (\xi^{co}n_{eff}^{co} - \xi^{cl}n_{eff}^{cl})\Delta T - \rho n_{eff}^{cl}\Delta RI \right] \quad (16)$$

By combining Equations (15) and (16), the temperature sensitivity and refractive index  $K_{val}^T$  and  $K_{val}^{RI}$  then:

$$\begin{cases} K_{val}^T = \frac{2L}{2k+1} (\xi^{co}n_{eff}^{co} - \xi^{cl}n_{eff}^{cl}) \\ K_{val}^{RI} = -\frac{2L}{2k+1} \rho n_{eff}^{cl} \end{cases} \quad (17)$$

Equation (17) explains that the blue color in the transmission spectrum will shift when the refractive index value increases while the red color in the transmission spectrum will shift when the temperature increases.

## 4. RESULTS AND DISCUSSION

### 4.1. Development of FO Use in Various Forms of Technology

Fiber optic sensors are a promising technology in various applications so that scientists develop the advantages of this fiber optic compared to using other methods. This review evaluates the current state of technology and explains the potential for significant use of fiber optic sensors and provides further explanation of how fiber optics will be used in the future [41-43].

### 4.2. Detection of Medical Devices

One of the developments of medical devices in detecting human movement is very important to do so that monitoring the performance of body organs as a whole and clinical care becomes easier. Periodic evaluation of atypical movements and vibrations in the stimulated hands so that they become early symptoms of deadly diseases such as Parkinson's, Alzheimer's and diabetes, provides convenience in early analysis and treatment of these diseases [42]. This study has developed a sensor that can be used to detect human movement forms on a large scale such as bending the legs, arms, hands and spine, and on a small scale such as fine muscle movements in the neck, chest and face through continuous signals [44].

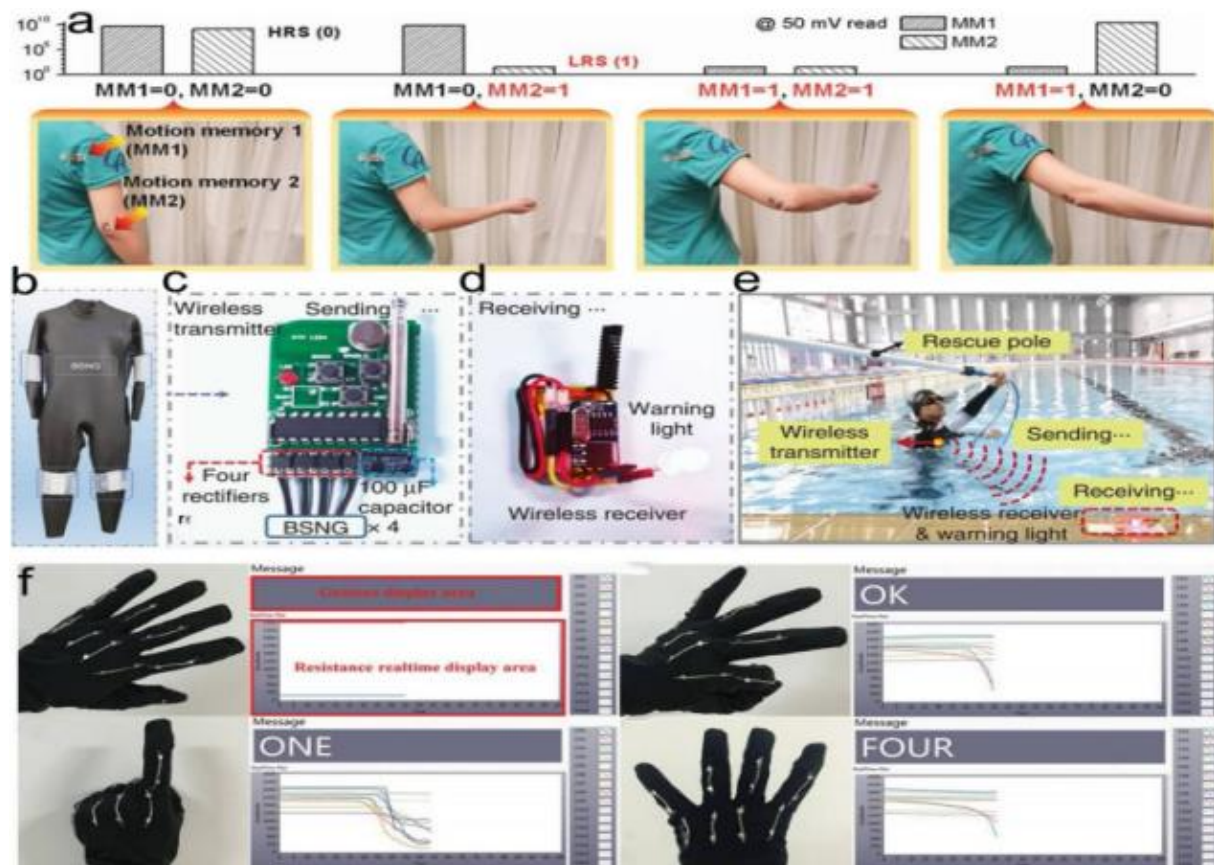


Figure 7. Image for: (a) monitoring of composite motion of elbow, shoulder abduction and elbow flexion with memory system [45]; (b) Optical image of BSNG system; (c) and (d) wireless transmitter and wireless receiver; (e) image of underwater rescue system [46]; and (f) difference of motion that corresponds to analog display detected on glove [47].

The development of this research uses hand and limb movements because the movements come from human life activities. This implementation makes this development quite promising because it is more efficient and easy to do. Previous studies used elastic devices made of neatly arranged SWCNT films. The SWCNT layer used must be large so that the detection of knee joint movement can be done. The study began by detecting the movement of the knee moving in one direction and rotating on its axis, then the knee was stretched and moved continuously so that the skin deformation changed constantly. The sensor can detect and distinguish various movements from stretching, bending the knee joint and bending, marching, squatting and jumping and several combinations of these movements [44]. New developments in strain sensors have been integrated with stretchable memory devices, some studies use human movement memory systems [45].

Figure 7 (a) shows that limb motion can be detected and stored in memory device by connecting to limb joints, so that deformation caused by limb motion can be read. Previous research used Bionic Stretchable Nanogenerator (BSNG) inspired by electric eel. BSNG integrated with transmission module and wireless transmission system for human body is built because it has good mechanical response, flexibility and output. This research can be seen in Figure 7b-e. In the research, there is a linear relationship between BSNG output voltage on human arm and elbow bend. This research also found that breaststroke has the largest motion amplitude signal compared to other styles caused by larger amplitude in arm and leg movements.

The study also explains the results of finger movements from each human movement. The use of flexible strain sensors and integration into gloves, finger movement monitoring can be detected as a whole. Changes in electrical parameters related to finger curvature can be found when finger movements stretch the sensor strip [48-50]. This study continued by developing a highly sensitive motion sensor based on the implantation of elastic microcapsules into bionic structures [48]. When the motion sensor is connected to the finger, pressure and strain can be detected simultaneously

continuously. The relative current increases gradually according to the angle of finger movement. This study uses MWCNT/TPE so that the sensor can operate in wet conditions because its surface is superhydrophobic. This sensor can detect differences in finger movement in real time by collecting changes in the resistance of each finger in the data acquisition system. This device can analyze signal changes and compare them with a configured database as shown in Figure 7f. 3. Civil Engineering Landslides are a significant hazard that can cause many casualties and property losses. Continuous measurement and time analysis of geotechnical parameters in geotechnical monitoring can detect anomalous behavior in the early phase [51-53]. Geotechnical inclinometers are used to determine the shape of landslides using the magnitude of direction, speed and depth. These parameters are very important in understanding landslide behavior and slope movement to develop intervention strategies [54]. The use of fiber optic sensors is very necessary because of its resistance to corrosion and the ability to detect shapes continuously without visual contact. The development of research on inclinometers focuses on the design of distributed multi-fiber optic inclinometers for monitoring ground motion by utilizing strain sensors embedded in tubes such as Figure 8 [53, 55]. This sensor has a cross-section with the same configuration as multicore fiber optics, but with a larger core distance to achieve better accuracy when measuring the curvature and shape of the sensor [56, 57].

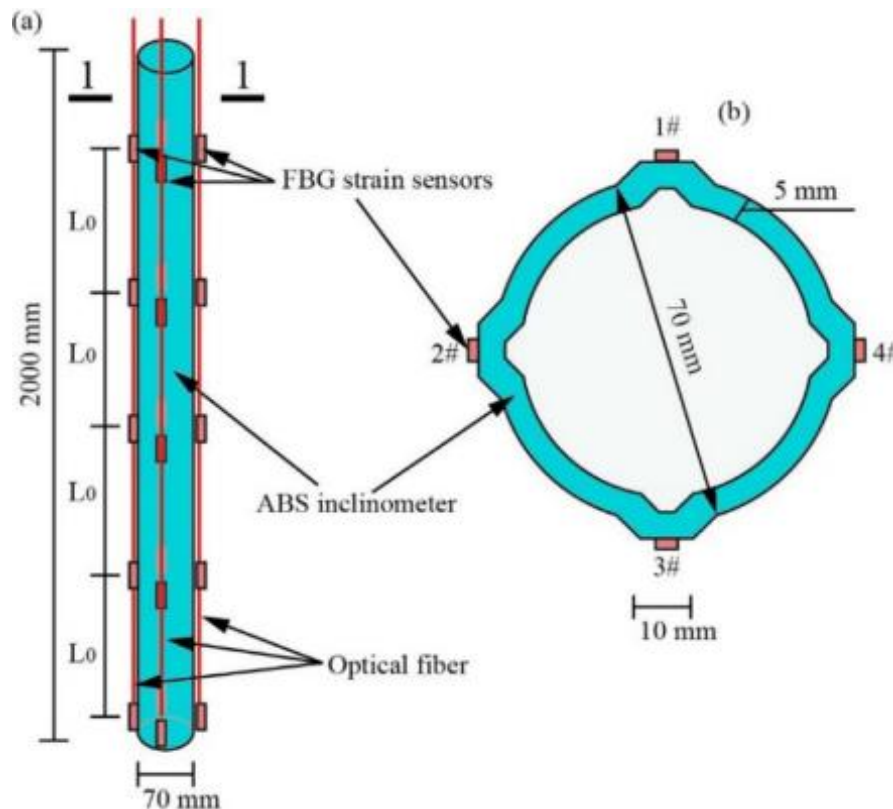


Figure 8. Image for: (a) FBG schematic on the inclinometer and (b) MFC diameter.

#### 4.3. Development of Surgical Equipment

Dynamic detection of shape and position to place medical equipment on the human body is very important in improving accuracy and minimizing invasiveness [58, 59]. Clinical procedures such as the use of fluoroscopy have several disadvantages including low data acquisition speed, high cost and high radiation exposure [57, 58, 60-63]. Fiber optic sensors have great advantages in various medical applications including colonoscopy [64-67] and epidural administration [61], eye and heart checks as seen in Figure 9 [66], biopsies [64, 66] endovascular navigation [65] and invasive surgery [62, 67-69]. The development of this optical fiber can be implemented efficiently in various medical devices such as needles, catheters, endoscopes because it has the advantages of embedding capabilities, biocompatibility, flexibility, light weight, small size, high regularity. In previous research, Lunwei et al in 2014 [70] made an intelligent colonoscopy consisting of FBG mounted on a 900 mm

long flexible wire. This sensor was implemented in a colonoscope and tested on the large intestine of a living pig, so that it was able to reconstruct the shape of the medical device. Then Bulan et al in 2014 designed a very flexible and thin FOSS so that it could be integrated into an invasive surgical system and was able to track dynamically and in real time (the speed of the sampling 3.74 Hz) with a position error of about 1.50% of the total length of the sensor [61]. This sensor is made by attaching three optical fibers where the FBG is planted in a triangle shape that has a length of 115 mm and can be bent up to 900. In 2014 Roesthuis developed a flexible nitinol (NiTi) needle and integrated from 12 FBG sensors in three-dimensional development [69]. This sensor can detect curvature, axial strain, maximum error shape between experiments and results based on beam theory of 0.20, 0.51 and 1.66 mm by taking into account deflection in single bending, double bending and external plane.

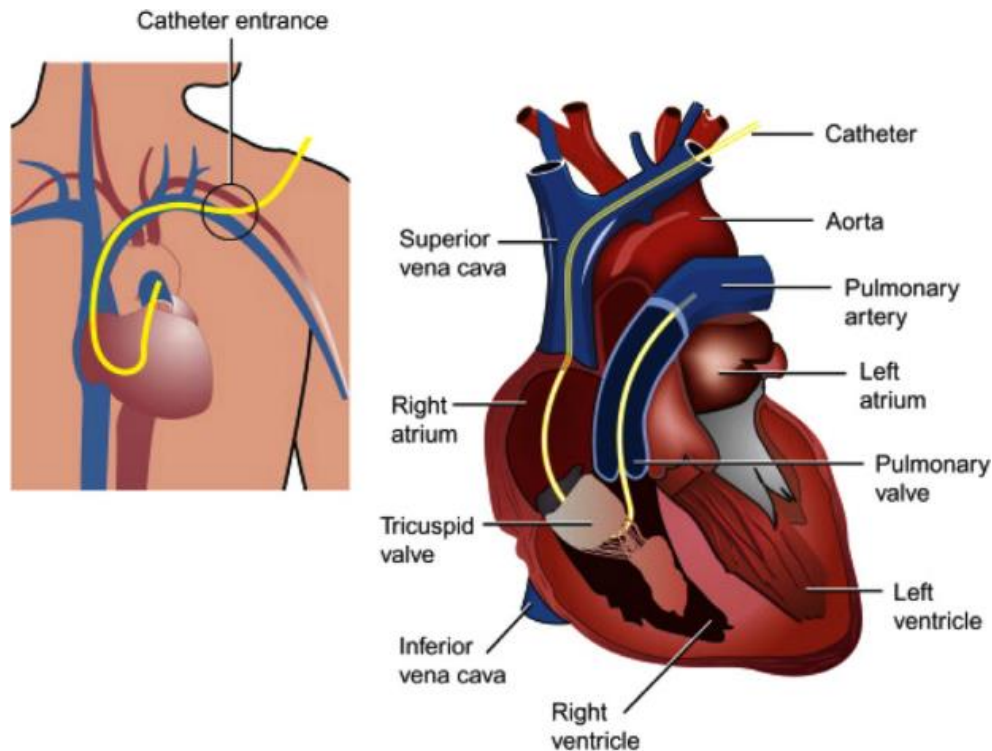


Figure 9. Thermistor catheter for temperature measurement in the pulmonary artery [68].

## 5. CONCLUSION

This review focuses on the development of fiber optic sensors from several application technologies. This development is actually based on the advantages that make the use of fiber optic sensors more competitive than the use of other sensors. This article presents a comprehensive review of the development of fiber optic sensors and their applications. The existence of a simple and easy way to measure temperature and mechanical strain and has bio-compatibility and biodegradability properties, causing the use of fiber optic sensors to be in great demand for non-invasive use in detecting parameters in medical applications such as body movement, body temperature, blood pressure, metabolites, and detecting vital signs of subjects that can be connected to passive or active electronic transmission modules, signal processing equipment, power supplies and interface displays via wireless. The use of interferometers in fiber optic sensors also increases accuracy, and has very high sensitivity and very fast response. This sensor also has advantages such as high coupling efficiency, low cost. This article also provides a detailed overview of the potential and inspiration for scientists and field technicians in the development of future research. All sensors in the future are expected to be quantum-based fiber optic sensors which are a promising alternative means for luminescence-based bioanalytical techniques, and can also be used in biomedical devices by developing the geometric properties of optical fibers.

## REFERENCES

- [1] Rosenthal, A., Razansky, D., & Ntziachristos, V. (2011). High-sensitivity compact ultrasonic detector based on a pi-phase-shifted fiber Bragg grating. *Optics Letters*, **36**(10), 1833–1835.
- [2] Wu, Q. & Okabe, Y. (2012). High-sensitivity ultrasonic phase-shifted fiber Bragg grating balanced sensing system. *Optics Express*, **20**(27), 28353–28362.
- [3] Lin, Z. T., Lv, R. Q., Zhao, Y., & Zheng, H. K. (2020). High-sensitivity salinity measurement sensor based on no-core fiber. *Sensors and Actuators A: Physical*, **305**, 111947.
- [4] Sun, B., Fang, F., Zhang, Z., Xu, J., & Zhang, L. (2018). High-sensitivity and low-temperature magnetic field sensor based on tapered two-mode fiber interference. *Optics Letters*, **43**(6), 1311–1314.
- [5] Yang, X., Shi, C., Wheeler, D., Newhouse, R., Chen, B., Zhang, J. Z., & Gu, C. (2010). High-sensitivity molecular sensing using hollow-core photonic crystal fiber and surface-enhanced Raman scattering. *Journal of the Optical Society of America A*, **27**(5), 977–984.
- [6] Wen, Z., Guan, Z., Dong, J., Li, H., Cai, Y., & Gao, S. (2022). A review of sensitivity enhancement in interferometer-based fiber sensors. *Sensors*, **22**(7), 2506.
- [7] Liang, L., Li, M., Liu, N., Sun, H., Rong, Q., & Hu, M. (2018). A high-sensitivity optical fiber relative humidity sensor based on microsphere WGM resonator. *Optical Fiber Technology*, **45**, 415–418.
- [8] Werneck, M. M. (2013). A guide to fiber bragg grating sensors, in current trends in shortand long period fiber gratings. *IntechOpen*, 1–24.
- [9] Yao, Q., Meng, H., Wang, W., Xue, H., Xiong, R., Huang, B., Tan, C., & Huang, X. (2014). Simultaneous measurement of refractive index and temperature based on a core-offset Mach-Zehnder interferometer combined with a fiber Bragg grating. *Sensors and Actuators A: Physical*, **209**, 73–77.
- [10] Bhardwaj, V., Kishor, K., & Sharma, A. C. (2020). Tapered optical fiber geometries and sensing applications based on Mach-Zehnder Interferometer: A review. *Optical Fiber Technology*, **58**, 102302.
- [11] Tong, Z., Wang, X., Wang, Y., Zhang, W., & Gong, M. (2017). Dual-parameter optical fiber sensor based on few-mode fiber and spherical structure. *Optics Communications*, **405**, 60–65.
- [12] Rajan, G., Liu, B., Luo, Y., Ambikairajah, E., & Peng, G. D. (2013). High sensitivity force and pressure measurements using etched singlemode polymer fiber Bragg gratings. *IEEE Sensors Journal*, **13**(5), 1794–1800.
- [13] Her, S. C. & Huang, S. Y. (2016). Thermal strain measured by fiber Bragg grating sensors. *Sens. Mater.*, **28**(9), 939–946.
- [14] Wu, W. & Liu, X. (2015). Investigation on high temperature characteristics of FBG sensors. *Optik*, **126**(20), 2411–2413.
- [15] Huang, Y., Azarmi, F., & Jazi, M. S. (2015). Composite coatings for fibre Bragg grating sensor in high temperature environments. *Int. J. Sens. Sens. Networks*, **3**(2), 12–17.
- [16] Pan, X., Dong, Y., Zheng, J., Wen, J., Pang, F., Chen, Z., Shang, Y., & Wang, T. (2019). Enhanced FBG temperature sensitivity in PbS-doped silica optical fiber. *Journal of Lightwave Technology*, **37**(18), 4902–4907.
- [17] Ju, S., Watekar, P. R., & Han, W. T. (2010). Enhanced Sensitivity of the FBG temperature sensor based on the PbO-GeO<sub>2</sub>-SiO<sub>2</sub> glass optical fiber. *Journal of Lightwave Technology*, **28**(18), 2697–2700.
- [18] Molardi, C., Paixão, T., Beisenova, A., Min, R., Antunes, P., Marques, C., Blanc, W., & Tosi, D. (2019). Fiber Bragg grating (FBG) sensors in a high-scattering optical fiber doped with MgO nanoparticles for polarization-dependent temperature sensing. *Applied Sciences*, **9**(15), 3107.
- [19] Mihailov, S. J. (2012). Fiber Bragg grating sensors for harsh environments. *Sensors*, **12**(2), 1898–1918.
- [20] Rosenberger, M., Hessler, S., Girschikofsky, M., Kefer, S., Belle, S., Hellmann, R., & Schmauss, B. (2018). High temperature stable polymer planar waveguide Bragg grating sensors. *2018 IEEE 7th International Conference on Photonics (ICP)*, 1–3.
- [21] Korganbayev, S., Min, R., Jelbuldina, M., Hu, X., Caucheteur, C., Bang, O., Ortega, B., Marques, C., & Tosi, D. (2018). Thermal profile detection through high-sensitivity fiber optic

- chirped Bragg grating on microstructured PMMA fiber. *Journal of Lightwave Technology*, **36**(20), 4723–4729.
- [22] Cook, K., Canning, J., Bandyopadhyay, S., Lancry, M., Martelli, C., Jin, T., & Csipkes, A. (2007). Technologies for high temperature fibre Bragg grating (FBG) sensors. *Technica*.
- [23] Girschikofsky, M., Rosenberger, M., Förthner, M., Rommel, M., Frey, L., & Hellmann, R. (2017). Waveguide Bragg gratings in Ormocer® s for temperature sensing. *Sensors*, **17**(11), 2459.
- [24] Laffont, G., Cotillard, R., & Ferdinand, P. (2013). Multiplexed regenerated fiber Bragg gratings for high-temperature measurement. *Measurement Science and Technology*, **24**(9), 094010.
- [25] Wang, L., Wang, Y., Wang, J., & Li, F. (2020). A high spatial resolution FBG sensor array for measuring ocean temperature and depth. *Photonic Sensors*, **10**, 57–66.
- [26] Tosi, D. (2017). Review and analysis of peak tracking techniques for fiber Bragg grating sensors. *Sensors*, **17**(10), 2368.
- [27] Wang, Y., Yuan, H., Liu, X., Bai, Q., Zhang, H., Gao, Y., & Jin, B. (2019). A comprehensive study of optical fiber acoustic sensing. *IEEE Access*, **7**, 85821–85837.
- [28] Her, S. C. & Lin, W. N. (2020). Simultaneous measurement of temperature and mechanical strain using a fiber Bragg grating sensor. *Sensors*, **20**(15), 4223.
- [29] Xie, M., Gong, H., Zhang, J., Zhao, C. L., & Dong, X. (2018). Optical fiber sensor based on Mach–Zehnder interferometer combined with a fiber Bragg grating for simultaneous measurement of refractive index and temperature. *Optical Engineering*, **57**(11), 117107.
- [30] Liu, Q., He, X., Fu, H., Yang, D., Xiao, F., & Wang, X. (2020). Temperature-insensitive optical fiber reflective micro-liquid level sensor base on the drop shape quasi-Mach Zehnder interferometer. *Optik*, **216**, 164893.
- [31] Chu, R., Guan, C., Bo, Y., Shi, J., Zhu, Z., Li, P., Yang, J., & Yuan, L. (2019). All-optical graphene-oxide humidity sensor based on a side-polished symmetrical twin-core fiber Michelson interferometer. *Sensors and Actuators B: Chemical*, **284**, 623–627.
- [32] Feng, D., Liu, M., Feng, W., & Li, B. (2020). Michelson liquid-level sensor based on cascaded no-core fiber and single-mode fiber structure. *Optik*, **206**, 163746.
- [33] Sousa, A. O., Marques, C. A., Nogueira, R., & André, P. S. (2017). Simplified method for passive optical network in-service fibre-fault monitoring based on fibre Bragg gratings. *Photonic Network Communications*, **34**, 149–154.
- [34] Yang, Y., Lu, L., Yang, F., Chen, Y., & Jin, W. (2015). The fiber optic Sagnac interferometer and its sensing application. *2015 Optoelectronics Global Conference (OGC)*, 1–6.
- [35] Gong, J., Shen, C., Xiao, Y., Liu, S., Zhang, C., Ding, Z., Deng, H., Fang, J., Lang, T., Zhao, C., & Chen, Y. (2019). High sensitivity fiber temperature sensor based PDMS film on Mach-Zehnder interferometer. *Optical Fiber Technology*, **53**, 102029.
- [36] Ahmad, H. & Dernaika, M. (2015). Stabilized single longitudinal mode fibre ring laser based on an inline dual taper Mach Zehnder interferometer filter coated with graphene oxide. *Optics Communications*, **341**, 140–146.
- [37] Huang, R., Ni, K., Ma, Q., & Wu, X. (2016). Refractometer based on a tapered Mach–Zehnder interferometer with Peanut-Shape structure. *Optics and Lasers in Engineering*, **83**, 80–82.
- [38] Huerta-Mascotte, E., Sierra-Hernandez, J. M., Mata-Chavez, R. I., Jauregui-Vazquez, D., Castillo-Guzman, A., Estudillo-Ayala, J. M., Guzman-Chavez, A. D., & Rojas-Laguna, R. (2016). A core-offset Mach Zehnder interferometer based on a non-zero dispersion-shifted fiber and its torsion sensing application. *Sensors*, **16**(6), 856.
- [39] Jiang, L., Yang, J., Wang, S., Li, B., & Wang, M. (2011). Fiber Mach–Zehnder interferometer based on microcavities for high-temperature sensing with high sensitivity. *Optics Letters*, **36**(19), 3753–3755.
- [40] Li, B., Jiang, L., Wang, S., Yang, J., Wang, M., & Chen, Q. (2012). High sensitivity Mach–Zehnder interferometer sensors based on concatenated ultra-abrupt tapers on thinned fibers. *Optics & Laser Technology*, **44**(3), 640–645.
- [41] Ge, G., Cai, Y., Dong, Q., Zhang, Y., Shao, J., Huang, W., & Dong, X. (2018). A flexible pressure sensor based on rGO/polyaniline wrapped sponge with tunable sensitivity for human motion detection. *Nanoscale*, **10**(21), 10033–10040.

- [42] Xia, S., Song, S., & Gao, G. (2018). Robust and flexible strain sensors based on dual physically cross-linked double network hydrogels for monitoring human-motion. *Chemical Engineering Journal*, **354**, 817–824.
- [43] Zhao, X. H., Ma, S. N., Long, H., Yuan, H., Tang, C. Y., Cheng, P. K., & Tsang, Y. H. (2018). Multifunctional sensor based on porous carbon derived from metal–organic frameworks for real time health monitoring. *ACS Applied Materials & Interfaces*, **10**(4), 3986–3993.
- [44] Ge, G., Huang, W., Shao, J., & Dong, X. (2018). Recent progress of flexible and wearable strain sensors for human-motion monitoring. *Journal of Semiconductors*, **39**(1), 011012.
- [45] Liu, Y., Liu, Z., Zhu, B., Yu, J., He, K., Leow, W. R., Wang, M., Chandran, B. K., Qi, D., Wang, H., Chen, G., Xu, C., & Chen, X. (2017). Stretchable motion memory devices based on mechanical hybrid materials. *Advanced Materials*, **29**(34), 1701780.
- [46] Zou, Y., Tan, P., Shi, B., Ouyang, H., Jiang, D., Liu, Z., Li, H., Yu, M., Wang, C., Qu, X., Zhao, L., Fan, Y., Wang, Z. L., & Li, Z. (2019). A bionic stretchable nanogenerator for underwater sensing and energy harvesting. *Nature Communications*, **10**(1), 2695.
- [47] Chen, S., Lou, Z., Chen, D., Jiang, K., & Shen, G. (2016). Polymer-enhanced highly stretchable conductive fiber strain sensor used for electronic data gloves. *Advanced Materials Technologies*, **1**(7), 1600136.
- [48] Wang, L., Jackman, J. A., Tan, E. L., Park, J. H., Potroz, M. G., Hwang, E. T., & Cho, N. J. (2017). High-performance, flexible electronic skin sensor incorporating natural microcapsule actuators. *Nano Energy*, **36**, 38–45.
- [49] Kanaparthi, S., & Badhulika, S. (2016). Solvent-free fabrication of a biodegradable all-carbon paper based field effect transistor for human motion detection through strain sensing. *Green Chemistry*, **18**(12), 3640–3646.
- [50] Kong, J. H., Jang, N. S., Kim, S. H., & Kim, J. M. (2014). Simple and rapid micropatterning of conductive carbon composites and its application to elastic strain sensors. *Carbon*, **77**, 199–207.
- [51] Jibson, R. W. (2011). Methods for assessing the stability of slopes during earthquakes—A retrospective. *Engineering Geology*, **122**(1-2), 43–50.
- [52] Shanmugam, G. & Wang, Y. (2015). The landslide problem. *Journal of Palaeogeography*, **4**(2), 109–166.
- [53] Lenke, P., Wendt, M., Krebber, K., & Glötzl, R. (2011). Highly sensitive fiber optic inclinometer: easy to transport and easy to install. *21st International Conference on Optical Fiber Sensors*, **7753**, 758–761.
- [54] Wang, Y. L., Shi, B., Zhang, T. L., Zhu, H. H., Jie, Q., & Sun, Q. (2015). Introduction to an FBG-based inclinometer and its application to landslide monitoring. *Journal of Civil Structural Health Monitoring*, **5**, 645–653.
- [55] Liu, H. L., Zhu, Z. W., Zheng, Y., Liu, B., & Xiao, F. (2018). Experimental study on an FBG strain sensor. *Optical Fiber Technology*, **40**, 144–151.
- [56] Miller, G. A. (2015). Fabrication of a multifiber optical inclinometer. *IEEE Photonics Technology Letters*, **27**(12), 1289–1292.
- [57] Li, J., Correia, R., Chehura, E., Staines, S., James, S. W., & Tatam, R. P. (2010). A fibre Bragg grating-based inclinometer system for ground movement measurement. *Fourth European Workshop on Optical Fibre Sensors*, **7653**, 202–205.
- [58] Merloz, P., Troccaz, J., Vouaillat, H., Vasile, C., Tonetti, J., Eid, A., & Plaweski, S. (2007). Fluoroscopy-based navigation system in spine surgery. *Proceedings of the Institution of Mechanical Engineers, Part H: Journal of Engineering in Medicine*, **221**(7), 813–820.
- [59] Shi, C., Luo, X., Qi, P., Li, T., Song, S., Najdovski, Z., Fukuda, T., & Ren, H. (2016). Shape sensing techniques for continuum robots in minimally invasive surgery: A survey. *IEEE Transactions on Biomedical Engineering*, **64**(8), 1665–1678.
- [60] Mahesh, M. (2001). Fluoroscopy: patient radiation exposure issues. *Radiographics*, **21**(4), 1033–1045.
- [61] Beisenova, A., Issatayeva, A., Tosi, D., & Molardi, C. (2018). Fiber-optic distributed strain sensing needle for real-time guidance in epidural anesthesia. *IEEE Sensors Journal*, **18**(19), 8034–8044.

- [62] Moon, H., Jeong, J., Kang, S., Kim, K., Song, Y. W., & Kim, J. (2014). Fiber-Bragg-grating-based ultrathin shape sensors displaying single-channel sweeping for minimally invasive surgery. *Optics and Lasers in Engineering*, **59**, 50–55.
- [63] Yi, X., Qian, J., Shen, L., Zhang, Y., & Zhang, Z. (2007). An innovative 3D colonoscope shape sensing sensor based on FBG sensor array. *2007 International Conference on Information Acquisition*, 227–232.
- [64] Khan, F., Denasi, A., Barrera, D., Madrigal, J., Sales, S., & Misra, S. (2019). Multi-core optical fibers with Bragg gratings as shape sensor for flexible medical instruments. *IEEE Sensors Journal*, **19**(14), 5878–5884.
- [65] Jäckle, S., Eixmann, T., Schulz-Hildebrandt, H., Hüttmann, G., & Pätz, T. (2019). Fiber optical shape sensing of flexible instruments for endovascular navigation. *International Journal of Computer Assisted Radiology and Surgery*, **14**, 2137–2145.
- [66] Beisenova, A., Issatayeva, A., Iordachita, I., Blanc, W., Molardi, C., & Tosi, D. (2019). Distributed fiber optics 3D shape sensing by means of high scattering NP-doped fibers simultaneous spatial multiplexing. *Optics Express*, **27**(16), 22074–22087.
- [67] Parent, F., Loranger, S., Mandal, K. K., Iezzi, V. L., Lapointe, J., Boisvert, J. S., Baiad, M.D., Kadoury, S., & Kashyap, R. (2017). Enhancement of accuracy in shape sensing of surgical needles using optical frequency domain reflectometry in optical fibers. *Biomedical Optics Express*, **8**(4), 2210–2221.
- [68] Baura, G. (2021). Catheters, bare metal stents, and synthetic grafts. *Med. Device Technol.*, **1999**, 165–192.
- [69] Roesthuis, R. J., Kemp, M., Van den Dobbelsteen, J. J., & Misra, S. (2013). Three-dimensional needle shape reconstruction using an array of fiber bragg grating sensors. *IEEE/ASME Transactions on Mechatronics*, **19**(4), 1115–1126.
- [70] Lunwei, Z., Jinwu, Q., Linyong, S., & Yanan, Z. (2004). FBG sensor devices for spatial shape detection of intelligent colonoscope. *IEEE International Conference on Robotics and Automation, 2004 (Proceedings. ICRA'04. 2004)*, **1**, 834–840.